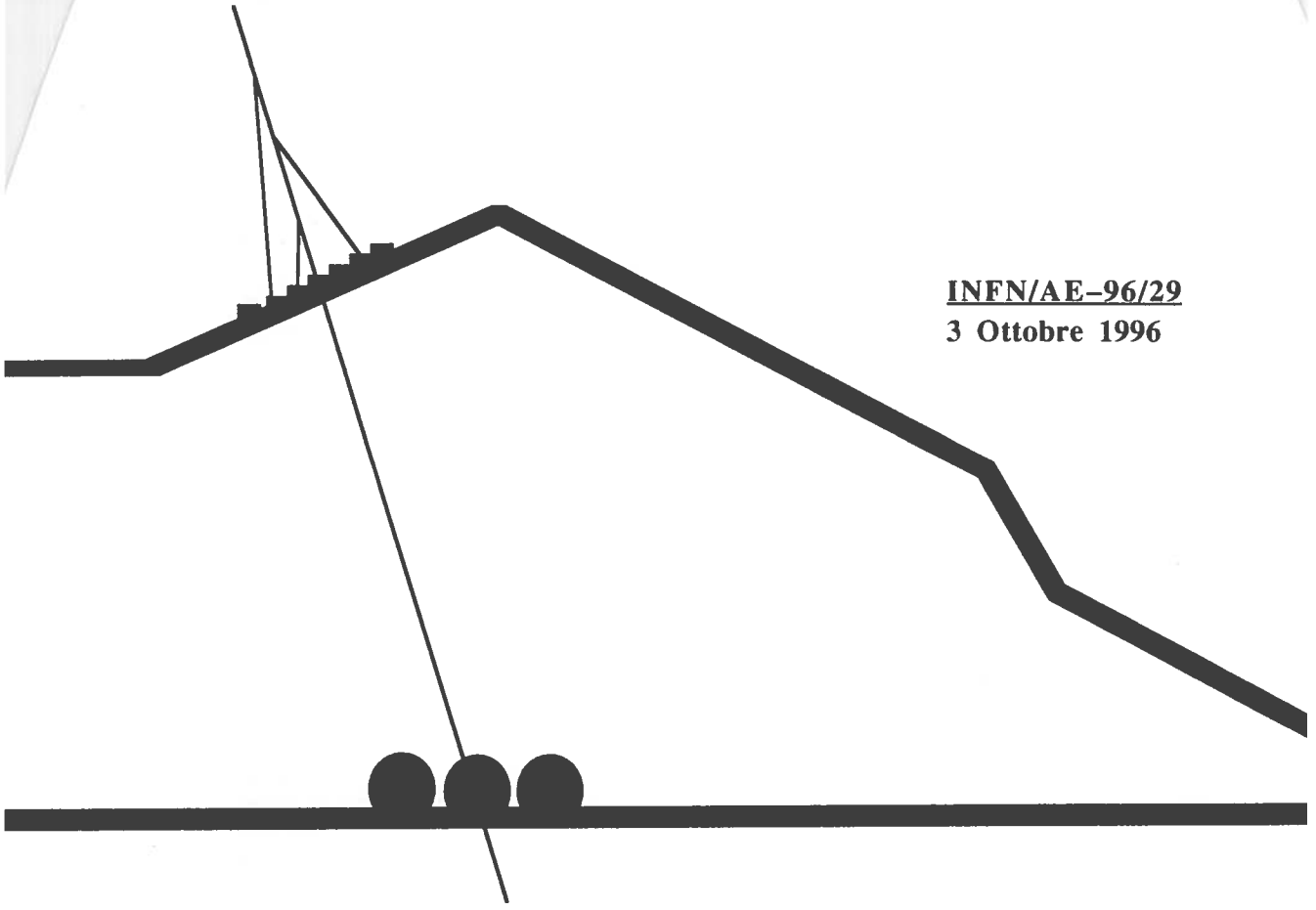

INFN/AE-96/29
3 Ottobre 1996

High Energy Cosmic Ray Physics with the MACRO Detector at Gran Sasso: Part II. Primary Spectra and Composition

The Macro Collaboration

Submitted to Physical Rewiew D

INFN - Laboratori Nazionali del Gran Sasso

INFN – Istituto Nazionale di Fisica Nucelare
Laboratori Nazionali del Gran Sasso

INFN/AE-96/29
3 Ottobre 1996

HIGH ENERGY COSMIC RAY PHYSICS WITH THE MACRO DETECTOR AT GRAN SASSO: PART II. PRIMARY SPECTRA AND COMPOSITION

The MACRO Collaboration

M. Ambrosio[12], R. Antolini[7], G. Auriemma[14,a], R. Baker[11], A. Baldini[13], G. C. Barbarino[12], B. C. Barish[4], G. Battistoni[6,b], R. Bellotti[1], C. Bemporad[13], P. Bernardini[10], H. Bilokon[6], V. Bisi[16], C. Bloise[6], T. Bosio[7], C. Bower[8], S. Bussino[14], F. Cafagna[1], M. Calicchio[1], D. Campana[12], M. Carboni[6], M. Castellano[1], S. Cecchini[2,c], F. Cei[13,d], V. Chiarella[6], A. Corona[14], S. Coutu[11], G. De Cataldo[1], H. Dekhissi[2,e], C. De Marzo[1], I. De Mitri[9], M. De Vincenzi[14,f], A. Di Credico[7], O. Erriquez[1], R. Fantini[2], C. Favuzzi[1], C. Forti[6], P. Fusco[1], G. Giacomelli[2], G. Giannini[13,g], N. Giglietto[1], M. Goretti[4,14], M. Grassi[13], A. Grillo[7], F. Guarino[12], P. Guarnaccia[1], C. Gustavino[7], A. Habig[8], K. Hanson[11], A. Hawthorne[8], R. Heinz[8], J. T. Hong[3], E. Iarocci[6,h], E. Katsavounidis[4], E. Kearns[3], S. Kyriazopoulou[4], E. Lamanna[14], C. Lane[5], D. S. Levin[11], P. Lipari[14], N. P. Longley[m], M. J. Longo[11], G. Mancarella[10], G. Mandrioli[2], A. Margiotta-Neri[2], A. Marini[6], D. Martello[10], A. Marzari-Chiesa[16], M. N. Mazziotta[1], D. G. Michael[4], S. Mikheyev[7,i], L. Miller[8], P. Monacelli[9], T. Montaruli[1], M. Monteno[16], S. Mufson[8], J. Musser[8], D. Nicoló[13,d], R. Nolty[4], C. Okada[3], C. Orth[3], G. Osteria[12], O. Palamara[10], S. Parlati[7], V. Patera[6,h], L. Patrizii[2], R. Pazzi[13], C. W. Peck[4], S. Petrera[10], P. Pistilli[10], V. Popa[2,l], A. Rainó[1], J. Reynoldson[7], M. Ricciardi[10], F. Ronga[6], U. Rubizzo[12], A. Sanzgiri[15], F. Sartogo[14], C. Satriano[14,a], L. Satta[6,h], E. Scapparone[7], K. Scholberg[4], A. Sciubba[6,h], P. Serra-Lugaresi[2], M. Severi[14], M. Sitta[16], P. Spinelli[1], M. Spinetti[6], M. Spurio[2], R. Steinberg[5], J. L. Stone[3], L.R. Sulak[3], A. Surdo[10], G. Tarlé[11], V. Togo[2], V. Valente[6], C. W. Walter[4] and R. Webb[15]

1. Dipartimento di Fisica dell'Università di Bari and INFN, 70126 Bari, Italy
2. Dipartimento di Fisica dell'Università di Bologna and INFN, 40126 Bologna, Italy
3. Physics Department, Boston University, Boston, MA 02215, USA
4. California Institute of Technology, Pasadena, CA 91125, USA
5. Department of Physics, Drexel University, Philadelphia, PA 19104, USA
6. Laboratori Nazionali di Frascati dell'INFN, 00044 Frascati (Roma), Italy
7. Laboratori Nazionali del Gran Sasso dell'INFN, 67010 Assergi (L'Aquila), Italy
8. Depts. of Physics and of Astronomy, Indiana University, Bloomington, IN 47405, USA
9. Dipartimento di Fisica dell'Università dell'Aquila and INFN, 67100 L'Aquila, Italy
10. Dipartimento di Fisica dell'Università di Lecce and INFN, 73100 Lecce, Italy
11. Department of Physics, University of Michigan, Ann Arbor, MI 48109, USA
12. Dipartimento di Fisica dell'Università di Napoli and INFN, 80125 Napoli, Italy
13. Dipartimento di Fisica dell'Università di Pisa and INFN, 56010 Pisa, Italy
14. Dipartimento di Fisica dell'Università di Roma "La Sapienza" and INFN, 00185 Roma, Italy
15. Physics Department, Texas A&M University, College Station, TX 77843, USA
16. Dipartimento di Fisica Sperimentale dell'Università di Torino and INFN, 10125 Torino, Italy
a Also Università della Basilicata, 85100 Potenza, Italy
b Also INFN Milano, 20133 Milano, Italy
c Also Istituto TESRE/CNR, 40129 Bologna, Italy
d Also Scuola Normale Superiore di Pisa, 56010 Pisa, Italy
e Also Faculty of Sciences, University Mohamed I, B.P. 424 Oujda, Morocco
f Also Dipartimento di Fisica, Università di Roma Tre, Roma, Italy
g Also Università di Trieste and INFN, 34100 Trieste, Italy
h Also Dipartimento di Energetica, Università di Roma, 00185 Roma, Italy
i Also Institute for Nuclear Research, Russian Academy of Science, 117312 Moscow, Russia
l Also Institute of Gravity and Space Sciences, 76900 Bucharest, Romania
m Swarthmore College, Swarthmore, PA 19081, USA

Multimuon data from the MACRO experiment at Gran Sasso have been analysed using a new method which allows one to estimate the primary cosmic ray fluxes. The estimated all-particle spectrum is higher and flatter than the one obtained from direct measurements but is consistent with EAS measurements. The spectral indexes of the fitted energy spectrum are 2.56 ± 0.05 for E<500 TeV and 2.9 ± 0.3 for E>5000 TeV with a gradual change at intermediate energies. The average mass number shows a weak dependence on the primary energy below 1000 TeV, with a value of 10.1 ± 2.5 at 100 TeV. Even within large uncertainties our data support a possible increase of the average mass number at higher energies. The fitted spectra cover a range from $\sim$ 50 TeV up to several thousand TeV.

1. Introduction

A characteristic feature of the cosmic ray spectrum is the steepening that occurs between 10^{15} and 10^{16} eV, the "knee" of the spectrum. Several explanations of this phenomenon have been offered, many of which lead to substantial differences in the predicted spectrum and composition near the knee. At present, cosmic rays below about $10^{14} \times Z$ eV are believed to be predominantly due to shock acceleration of particles by supernova blast waves in the interstellar medium [1]. At higher energies different mechanisms have been proposed, mainly involving acceleration from compact sources, like X-ray binaries or young supernova remnants [2]. More recently explosions of massive stars into their former stellar wind have been suggested as extensions of the basic supernova mechanism that could account for the whole knee region of cosmic ray spectrum [3]. Furthermore, the propagation and diffusion of cosmic rays in the Galaxy is generally considered to play a major role in the change of composition around the knee [2]. Therefore the interpretation of the knee is crucial in understanding the origin of the cosmic rays and may provide deeper insight into galactic acceleration and propagation phenomena.

Air shower arrays, air-Cherenkov telescopes and underground experiments can measure the whole region around the knee. In these indirect measurements the nature of the primary and its energy are inferred from the surface measurements of extensive air showers or from underground studies of the penetrating high energy muon component. Since the first observation of the knee [4] several experiments have measured the primary spectrum [5–10], confirming its general features. However the uncertainties in the conversion of the observed shower parameters (e.g. shower size, muon size, etc.) to primary energy and in the normalization of the spectrum make it difficult to extract precise features of the spectrum and composition.

MACRO multimuon events have been used in previous analyses [11–13] to study the primary cosmic ray composition by comparing the measured muon multiplicity distribution with that calculated using trial models of the primary spectrum and composition. These analyses, whose main purpose is to investigate the sensitivity of MACRO to composition, showed that MACRO data are inconsistent, at high multiplicities, with the predictions of an asymptotically Fe-dominated composition, like the Heavy composition [14], and favor a lighter model. MACRO data are reasonably explained by models with flat or slowly increasing $< A >$ as a function of the primary energy, as with the Light [14], CMC [15] and Σ [16] models, except for the absolute rates, where a factor of ~ 25 % is missing in the simulations. A similar analysis has been performed on MACRO data in coincidence with the EAS-TOP array detector [16].

In the present analysis we describe a new approach for measuring the primary spectrum and composition, using a multi-parametric fit of the MACRO data. The goal of this study is to obtain a model of the chemical composition of primary cosmic rays with energies between 10^{14} and 10^{17} eV. A wide energy interval of about one decade below the knee is available where direct measurements and underground measurements of the primary cosmic ray composition overlap. In our fitting procedure data from direct experiments are used as starting points to constrain the composition below the knee.

In the next section we describe the details of the Monte Carlo simulation of multiple muons and analyse the possible sources of systematic uncertainties in our simulation. The third section presents the multi-parametric fit procedure. In section 4 and 5 we give the primary spectrum and composition arising from the fitting procedure. In section 6 the MACRO experimental data on muon decoherence and vertical muon intensity are compared with the predictions of the fitted composition model. Section 7 discusses results and systematic uncertainties. Conclusions are given in section 8. Appendix addresses technical features of the adopted best fit method.

2. Monte Carlo simulation

The interpretation of deep underground muon data requires a simulation which includes a hadronic interaction model, the air shower development, the propagation of muons through the rock and a detailed description of the detector.

The procedure to get usable Monte Carlo predictions is complex and heavily CPU time consuming. In our analysis the following simulation strategy has been adopted. In the event generation, after sampling mass, energy and direction of the primary particle, event by event, the relevant kinematic variables are calculated for muons surviving underground. This event production pass covers a wide energy spectrum, from a few TeV up to 10^5 TeV and the full solid angle up to a zenith angle of 60 degrees. The upper limit at 10^5 TeV is motivated by the fact that only a few events per year are expected in our data sample at higher energies. For each event the impact position of shower axis is randomized over an area much larger than that of the detector. If at least a segment of track enters the acceptance area of MACRO, a detailed simulation of detector and trigger is started. This simulation, based on the GEANT [18] code, includes a detailed description of all the known physics and detector effects (electromagnetic showering down to 500 KeV, charge induction of the streamer signal onto the strips, electronic noise, *etc.*), and reproduces the experimental data at a satisfactory level of accuracy [17]. A final pass of the M.C. sequence processes the simulated data through the standard MACRO analysis program to reconstruct muon tracks and other related quantities.

An important step of our fit analysis was the reduction of this huge amount of simulated data into suitable functions allowing a fast calculation of the muon rates. The muon rates at any detected multiplicity N_μ are given by:

$$\begin{aligned} R(N_\mu) = \quad & \textstyle\sum_A \int_\Omega d\Omega \quad \int_S dS \int dE \; \Phi_A(E) \\ & \times \textstyle\sum_{M_\mu \geq N_\mu} \quad \mathcal{P}_A(E,\theta,\phi,M_\mu) \\ & \qquad\qquad\quad \mathcal{D}(\{\vec{r}_i\}_{X_o}; M_\mu \rightarrow N_\mu) \end{aligned} \tag{1}$$

where E, A and (θ,ϕ) denote the energy, mass number and incident direction of the primary nucleus, whose spectrum is represented by the function $\Phi_A(E)$. S represents the sampling area of the impact position of the shower axis, X_o, and Ω is the accepted solid angle. $\mathcal{P}_A(E,\theta,\phi,M_\mu)$ is the probability for a primary nucleus with physical parameters E,

through the rock only. $\mathcal{D}(\{\vec{r_i}\}_{X_o}; M_\mu \rightarrow N_\mu)$ depends on the muon bundle configuration and location inside the sampling area and on the detector geometry, acceptance and overall reconstruction efficiency.

The sample of simulated data allows us to calculate the functions $D_A(E, N_\mu)$

$$\begin{aligned} D_A(E, N_\mu) = \quad & 1/(\Omega S) \quad \int_\Omega d\Omega \int_S dS \\ & \times \textstyle\sum_{M_\mu \geq N_\mu} \quad \mathcal{P}_A(E, \theta, \phi, M_\mu) \\ & \qquad\qquad \mathcal{D}(\{\vec{r_i}\}_{X_o}; M_\mu \rightarrow N_\mu) \end{aligned} \tag{2}$$

which represent the probabilities (averaged over Ω and S) for a primary of mass A and energy per nucleus E to be reconstructed as an event with N_μ muons in MACRO. Making use of these functions the muon rates are expressed by the energy convolution integral:

$$R(N_\mu) = \Omega S \sum_A \int dE \; \Phi_A(E) \cdot D_A(E, N_\mu) \tag{3}$$

For this analysis, ~ 400 million events have been generated, subdivided in five $Log_{10}(E)$ bands, as follows: $3.8 \cdot 10^8$ primary nuclei ($1.1 \cdot 10^6$ underground muon events) between 3 and 20 TeV, $3.4 \cdot 10^7$ ($1.7 \cdot 10^6$) between 20 and 200 TeV, $3.6 \cdot 10^6$ ($1.1 \cdot 10^6$) between 200 and 2,000 TeV, $4.9 \cdot 10^5$ ($4.3 \cdot 10^5$) between 2,000 and 20,000 TeV and $4.6 \cdot 10^3$ ($4.3 \cdot 10^3$) between 20,000 and 100,000 TeV. The CPU time increases with energy from $\sim$1 s·MIPS/event[1] in the lowest energy band up to $\sim$1000 s·MIPS/event in the highest one. As a whole, one simulated hour of MACRO livetime requires a CPU time of $\sim$ 380 (MIPS·hours).

We assumed that primaries can be described using five mass groups (H, average mass A=1; He, average mass A=4; CNO, average mass A=14; Mg, average mass A=24; Fe, average mass A=56). The D_A functions have been calculated as 25×40 ($Log_{10}(E/GeV)$,N_μ) tables for each mass group, with N_μ ranging from 0 to 39 and $Log_{10}(E/GeV)$ from 3 to 8. The choice of the sizes of these tables is of crucial importance in the fit procedure we are going to describe in section 3. Our choice is a compromise of having a fine sampling of primary energies and muon multiplicities and a tolerable size of the simulated event sample. We established that this table size allows us to obtain, inserting the tabulated D_A functions in equation (3), muon multiplicity distributions as accurate as from direct use of simulated events, for any fixed composition.

There are some systematic uncertainties in the Monte Carlo predictions that have been investigated in detail. These include: uncertainties in the hadronic interaction model, in the knowledge of the map of the rock around MACRO and muon propagation through the rock.

2.1. Models of hadronic interactions

The simulation of the hadronic interactions of primary cosmic rays with air nuclei plays an essential role in the interpretation of indirect cosmic ray data. The present analysis has been mainly based upon the HEMAS [19] shower code. It contains a hadron interaction event generator based on the parameterization of minimum bias events at the Sp$\bar{p}$S collider by the UA5 experiment [20], generalized to nuclear targets. Multiplicity and pseudorapidity distributions reproduce collider data in the central region up to $\sqrt{s} \leq 900$

shower program which follows the shower development in the atmosphere with an energy cut on secondary particles down to 0.5 TeV. It also includes code for three-dimensional muon propagation in the rock.

The results this code have been parameterized [19] to provide a fast generator for underground muon physics. This parameterization has been used for the first analyses of MACRO experiment [12, 11, 21, 22], ignoring the correlation between muon multiplicity and lateral distribution. The need of a better comprehension of the underlying processes, and of understanding the associated systematics has lead to the use of the full code for the MACRO analysis.

In the present analysis, a series of improvements have been implemented in the Monte Carlo simulation. The pure superposition model has been replaced with the more realistic semi-superposition model [23]. At a given energy, this causes larger fluctuations than those obtained with the superposition model, but the average values of the main observables remain the same. The effect of the geomagnetic field has been introduced for the high energy muons in the shower code, wher the muon charge sign is randomly assigned. Charm hadroproduction has been also considered via insertion of a simple heavy flavor generator[2] to the standard hadron interaction routine of the HEMAS code. The contribution of charmed events to underground muons turned out to be negligible (of the order of a percent or less) on muon rates and of the order of a few percent on muon pair separations. Similar results have been obtained in ref.[25], using DPMJET [26] hadronic interaction model, where charm production is included. For this reason the heavy flavor generator was excluded from this composition analysis.

Fig. 1 shows the inclusive probabilities $P_A(E, M_\mu \geq 1)$ of having at least one detectable muon at MACRO, as a function of the primary energy, for the five elemental groups used in our simulation. $P_A(E, M_\mu \geq 1)$ is related to $\mathcal{P}_A(E, \theta, \phi, M_\mu)$ through the relationship:

$$P_A(E, M_\mu \geq 1) = 1/\Omega \int_\Omega d\Omega \sum_{M_\mu \geq 1} \mathcal{P}_A(E, \theta, \phi, M_\mu) \tag{4}$$

At least one muon underground has been requested in this plot, and this determines the increasing low energy limit when the mass group changes from hydrogen to iron. This has the consequence that heavier primaries are ineffective at lower energies, full efficiencies being reached roughly in the knee region. Furthermore at these higher energies heavy elements are more prolific than protons in producing underground muons.

In order to estimate the dependence of our results on the adopted event generator, we have also used the SIBYLL interaction model [27]. This work has been done mostly for comparison on a reduced sample of simulated events. The SIBYLL event generator has been inserted in the same shower code already used for HEMAS. The SIBYLL model is more physically motivated than the HEMAS simulation, being based on the dual parton model [28] with the inclusion of hard processes such as mini-jet production [29]. In the

[2] $c\bar{c}$ pairs have been assumed to be produced independently one of each other (uncorrelated production) with a differential cross section:

$$d^2\sigma/dx_F dp_T^2 \propto (1 - |x_F|)^\alpha \times exp(-\beta p_T^2)$$

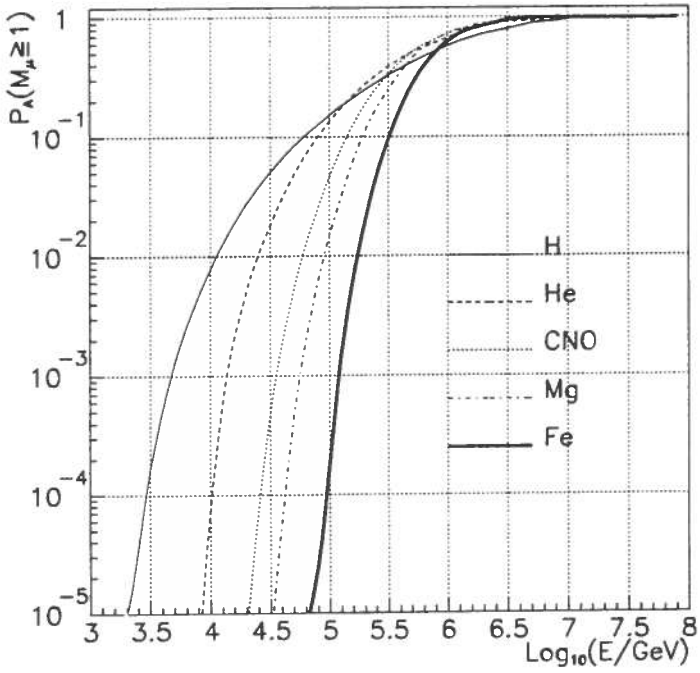

Figure 1. *Probabilities to give at least one muon at MACRO depth, calculated with HEMAS code.*

future other models will be considered, such as the DPMJET code [26], which has a more complete treatment of nuclear effects than does SIBYLL.

Fig. 2 shows, for each elemental group, the relative differences between SIBYLL and HEMAS average muon multiplicities at MACRO (full circles). It can be easily recognized that SIBYLL more effectively produces detectable muons near the underground muon production threshold, whereas at higher energies it approaches HEMAS. This behavior mainly affects the single muons (and the inclusive muon rates) since, at threshold, single muons dominate over multiple muons (open circles).

The multiplicity distributions of muons at MACRO depth have a similar behavior, with single muons slightly higher in SIBYLL and multiple muons slightly higher with HEMAS. Table 1 shows the relative differences between muon rates as obtained with SIBYLL and HEMAS for two different compositions ("Light", proton rich, and "Heavy", iron rich, [14]), at different N_μ intervals. The Light and Heavy compositions are extreme models: at increasingly higher energies the Light composition contains a large proton component while the Heavy composition contains a large Fe component. Therefore, even with a drastic change in the composition spectra, the relative difference between the muon rates obtained in the framework of the two interaction models is always at most $\sim$ 7 %. It has to be noted that it mainly affects muon rates at low multiplicity, for which the statistical errors are very small. Comparative analyses [30][27][31] among various

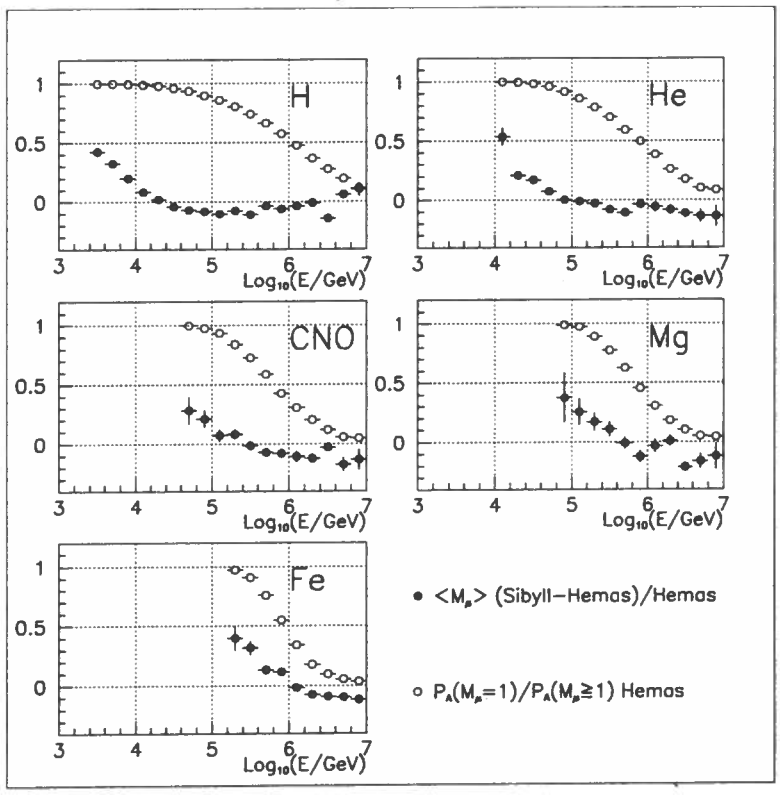

Figure 2. *Full circles: relative differences between SIBYLL and HEMAS average muon multiplicities at MACRO: (S-H)/H. Open circles: fraction of single muons as with HEMAS code.*

to currently available models. Possible inadequacies of existing interaction models will be discussed at larger extent in sect. 7.

2.2. Rock depth around MACRO

The analysis of the vertical muon intensity measured in MACRO [32, 17] has motivated a detailed study of the systematic uncertainties in the rock depth above MACRO. The rock depth h (in m.w.e.) in each direction is obtained by multiplying the rock thickness by the average Gran Sasso rock density (2.71 ± 0.05 g/cm^3) [17]. The systematic uncertainties on h have two main sources:

- the uncertainties in the knowledge of the topographical map of the Gran Sasso region and in the interpolation procedure to transform it to a function of the zenith and azimuth angles;
- the assumption of a homogeneous mountain instead of a more realistically stratified structure [33].

The first term mainly causes point to point uncertainties of the order of few percent

Table 1
Relative differences between SIBYLL and HEMAS muon rates: (S-H)/H. The values are given for the Light and Heavy compositions (see text).

Composition	M_μ=1	M_μ=2 ÷ 6	M_μ>6	$M_\mu \geq 1$
Light [14]	0.058 ± 0.003	-0.08 ± 0.01	-0.07 ± 0.05	0.048 ± 0.003
Heavy [14]	0.072 ± 0.004	-0.03 ± 0.01	-0.02 ± 0.02	0.064 ± 0.003

We have investigated the effect on the Monte Carlo predictions introduced by a net change of the rock depth by -1%, -2% and -5% everywhere, as originating from an average density uncertainty. The multimuon rates increase by ∼+5%, ∼+10% and ∼+25%, respectively, roughly independently of the muon multiplicity. In other words a net change of the rock depth, within the limits compatible with our rock uncertainties, affects the rates $R(N_\mu)$, but not the rates normalized to the singles, i.e. $r(N_\mu) = R(N_\mu)/R(1)$. To show this, in fig. 3 the relative differences of $r(N_\mu)$, obtained with different average rock densities, with respect to the one at the Gran Sasso nominal density, are plotted as a function of the muon multiplicity. One can easily recognize that, within the statistical uncertainties of simulated data, $r(N_\mu)$ is roughly the same at any rock density and compatible with being independent of N_μ. This fact reflects the loose, but in spite of that effective, correlation between muon energy and primary energy, which is not considered when these effects are analysed only considering the muon survival probability.

2.3. Muon propagation through the rock

The original HEMAS code for the muon propagation through the rock (described in ref. [19]) has been compared with the codes by Lipari and Stanev [34] and FLUKA[35]. The main differences of these codes with the original HEMAS muon propagation code is a more accurate treatment of the muon stochastic energy loss and of the radiative processes. Some theoretical uncertainties are anyway still present in the treatment of the radiative processes considered in the FLUKA and Lipari-Stanev codes. Moreover uncertainties remain about the choice of the screening function used in the bremsstrahlung cross section.

Monte Carlo simulations show that while the uncertainties from the muon propagation affect the absolute muon rates at a level of ∼8 % they do not affect the shape of multiplicity distributions.

3. Multi-parametric fit of the composition parameters

In this analysis a minimization procedure is used to estimate the primary cosmic ray composition from the best fit of the MACRO experimental rates of multimuon events. Previous underground experiments have been able to perform only very simple fits (with only one free parameter) of experimental data [36][37] in order to obtain information about primary composition. The main reason for that was the small detection area of their experimental apparata, so that only a small fraction of the muons in a high multiplicity event was seen by these detectors. On the contrary, the large acceptance of the MACRO

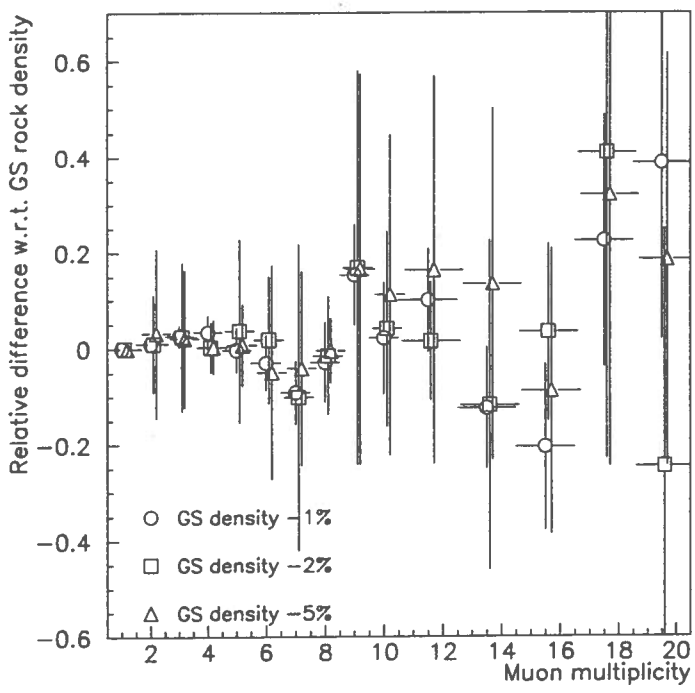

Figure 3. *Relative differences of $r(N_\mu)$ at different average rock densities with respect to the one at at the Gran Sasso nominal density.*

In our fitting procedure, the predicted rates of events with N_μ reconstructed muons, $R(N_\mu)$, are calculated using formula (3). $\Phi_A(E)$ are the differential primary cosmic ray fluxes of the nuclei of mass A we aim to estimate, while the $D_A(E, N_\mu)$ functions are tabulated functions derived by our full Monte Carlo simulation. We assume that the energy spectrum of each elemental group can be expressed by simple power laws whose spectral indexes change at a mass dependent cutoff energy, $E_{cut}(A)$:

$$\Phi_A(E) = K_1(A)E^{-\gamma_1(A)} \qquad \text{for } E < E_{cut}(A) \tag{5}$$

$$\Phi_A(E) = K_2(A)E^{-\gamma_2(A)} \qquad \text{for } E > E_{cut}(A) \tag{6}$$

with $K_2 = K_1 E_{cut}^{\gamma_2-\gamma_1}$. This correspond to 4 free parameters $(K_1, \gamma_1, \gamma_2, E_{cut})$ to be determined for each elemental primary spectrum that we want to estimate.

We minimize the function:

$$\chi^2_M = \sum_{N_\mu} \frac{[R^{meas}(N_\mu) - R(N_\mu \mid parameters)]^2}{\sigma^2[R^{meas}(N_\mu)] + \sigma^2[R(N_\mu \mid parameters)]} \tag{7}$$

where $R^{meas}(N_\mu)$ are 39 experimental points of MACRO multiplicity distribution [17],

ray spectra are obtained from the estimate of the parameters at the minimum of the function (7). The errors on the spectra are calculated using the covariance matrix of the parameters.

The function minimization has been done using the MINUIT [38] package, a widely used application designed to compute the best-fit parameter values and uncertainties, including correlations between the parameters.

3.1. Preliminary tests

Using five mass groups (H, He, CNO, Mg, Fe), we have 20 parameters to be fitted using formula (7). Such a high number of free parameters and the dependence of the muon rates on the composition parameters, through a convolution of primary spectra over a wide energy range, makes it difficult to estimate the primary composition using the procedure described above (see also Appendix A). Before going through the complexity of a minimization with so many parameters, we performed preliminary tests, assuming simplified hypotheses of primary compositions, which allow us to reduce the number of free parameters to be fitted. In particular we checked if our multiplicity distribution was compatible with pure compositions or with compositions with only groups of elements.

With the assumption of a pure primary composition (only 4 free parameters), which is the simplest composition hypothesis that can be done, the minimization procedure does not converge for any primary mass. Therefore our data rule out the hypothesis of pure compositions, such as extreme proton or iron pure compositions. Obviously a pure iron composition predicts too few low multiplicity events and too many high multiplicity events, whereas a pure proton composition can fit the integral muon rate properly, but predicts too few high multiplicity events.

The assumption of pure compositions is inadequate to represent the whole multiplicity distribution, since the different mass groups do not play the same role in the various multiplicity regions. Fig.4, which shows the contributions of the elemental groups to the multiplicity distribution calculated from the Monte Carlo simulation using different composition models, indicates that low multiplicity events mostly come from protons and Helium nuclei, while high multiplicity events reflect much heavier primaries. Moreover low multiplicity events come from primaries with energies less than few hundred TeV (below the knee), while high multiplicity events are produced by primaries in an energy region which includes the knee [12]. We therefore fitted the low multiplicity part (N_μ=1÷6) of our experimental multiplicity distribution using only light (H+He) elements and assuming single power law energy spectra (corresponding to 4 free parameters) . The remaining part of the distribution ($N_\mu > 6$) has been fitted independently with heavier mass groups (CNO+Mg+Fe), assuming two power law spectra (corresponding to 12 free parameters). In both cases the multi-parametric fit procedure converges. The minimum $\chi^2_M/D.o.F.$ is 1.7 for the low multiplicity fit and 0.5 for the high multiplicity fit. These results confirm qualitatively the dominance of different elemental groups at different multiplicities, but do not allow to give their spectra in the whole primary energy range. In fact the loose correlation between muon multiplicity and primary energy prevents us from merging the spectra arising from the two separate fits.

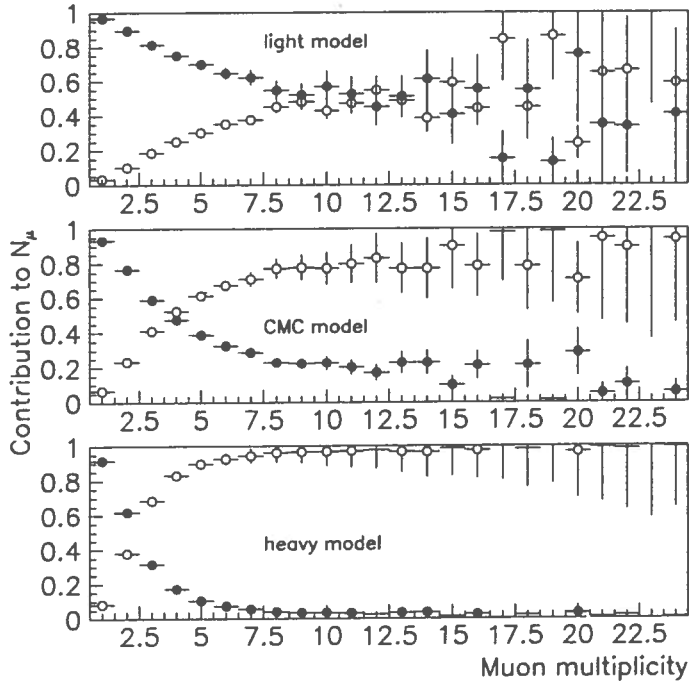

Figure 4. *Contribution of (H+He) (full circles) and (CNO+Mg+Fe) (open circles) groups to the multiplicity distribution for the Light, CMC and Heavy composition models*

in the whole multiplicity range of MACRO data. The ability of our best fit procedure to reconstruct primary compositions based on five elemental groups is described separately in Appendix E.

In order to get successful fits with five mass groups we are forced to reduce the number of free parameters. Constraints in the fit procedure, which reduce the number of free parameters, can be achieved by making physical assumptions on composition parameters. A wide class of composition models attributes the cutoff in the primary energy spectrum to particle leakage in the Galaxy at fixed magnetic rigidity [39]. We adopted this physical hypothesis in our fit, assuming that the energy cutoffs of elemental groups follow the relationship:

$$E_{cut}(Z) = E_{cut}(Fe) \cdot Z/26 \tag{8}$$

With this hypothesis the number of free parameters is 16 and the number of degree of freedom of χ^2_M is ν_M=23.

Using this condition, the minimization of the χ^2_M function (7) turns out to be successful, if we impose suitable limits on the parameters in order to prevent them from taking on unphysical values because of numerical difficulties in the calculation of the minimized function of formula (7). The parameter space has been bounded taking into

from those obtained in a more complete analysis of cosmic ray direct data [43]. Allowing $\gamma_1(A)$ and $K_1(A)$ to be limited within $\pm 5\ \sigma$ of their best fit values obtained from direct measurements, $\gamma_2(A) = 2.8 \div 3.2$, and $Log_{10}(E_{cut}(Fe)/GeV) = 6 \div 7.5$ the minimization of MACRO data points (7) is successful and the minimum is reached at $\chi^2_M/D.o.F$=13/23~0.6. However, as explained in Appendix A, boundary conditions are generally undesired, since the parameters can be correctly estimated, but with unreliable errors due to numerical problems in the calculation of the covariance matrix.

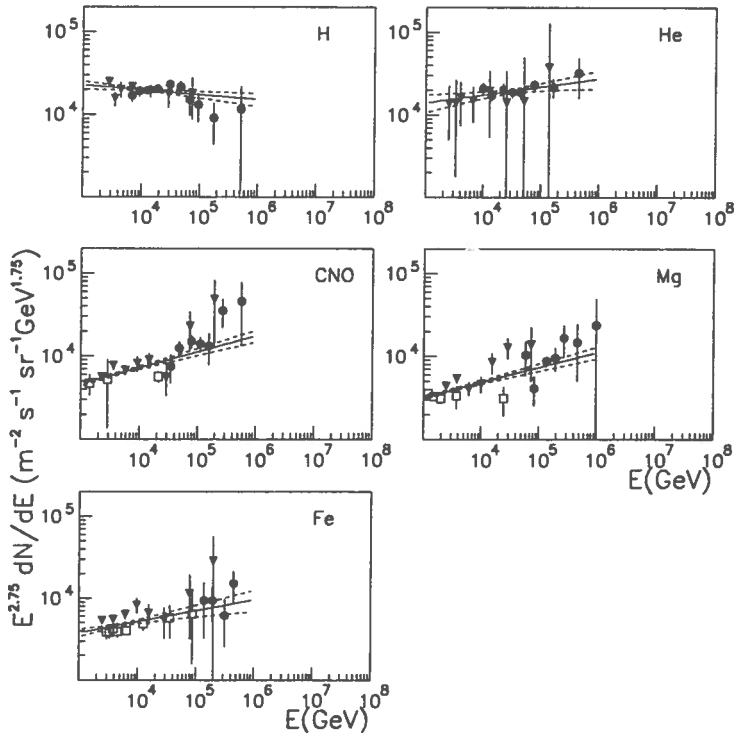

Figure 5. *Measurements of primary cosmic ray energy spectra from recent direct experiments. Full circles: JACEE [40], full triangles: Sokol [41], open squares: CRN [42]. Primary spectra resulting from a fit of experimental points with single power law spectra are also shown (solid line: best fit value; dashed line $\pm 1\sigma$ error).*

For this reason we preferred to use a different approach. MACRO multimuon events are produced by primaries in the energy range of ~ 50 to $\sim 10^5$ TeV [11–13]. A wide energy interval of about one decade below the knee is available where direct measurements and underground measurements overlap. Therefore we inserted direct measurements in the minimization function so that they can act as starting points and constrain the primary spectra below the knee. For this purpose the minimization function has been redefined as follows (see Appendix A):

Table 2
Direct measurement contributions to the fitting procedure.

λ_D	direct measurement contribution
1	91/130∼0.70
0.5	0.5·91/85∼0.54
0.1	0.1·91/48∼0.19
0.01	0.01·91/40∼0.02

direct flux measurements:

$$\chi^2_D = \sum_A \sum_{i=1}^{N_A} \frac{[\Phi_A^{meas}(E_i) - \Phi_A(E_i \mid parameters)]^2}{\sigma^2[\Phi_A^{meas}(E_i)]}. \quad (10)$$

λ_M and λ_D are fixed weight parameters, and $\Phi_A(E_i \mid parameters)$ are the primary cosmic ray fluxes of the nucleus A at fixed primary energies E_i, defined by formula (5). In the χ^2_D term we used 91 $\Phi_A^{meas}(E_i)$ data points [40][41][42] (N_A for each elemental group, at different E_i energies), the same that are shown in fig. 5. This corresponds to a number of degree of freedom ν_D=75, using the rigidity cut hypothesis (8).

In our fitting procedure we set λ_M=1 and we performed independent ξ^2 minimizations at different values of λ_D within λ_D = 1 and 0.01, corresponding to different constraining power of the direct measurements to MACRO data. Under these conditions the minimization is successful and the calculation of the covariance matrix is accurate, at any λ_D value, without parameter limits. The number of "equivalent data points" used in the multi-parametric fit procedure is roughly given by 39 + λ_D· 91. The contribution of the direct measurements to the fitting procedure, varying λ_D from 1 to 0.01, is reported in Table 2. In this range of weight parameters, the ξ^2 function is equivalent to a χ^2 variable with $\nu_M + \lambda_D \cdot \nu_D$ degrees of freedom (see Appendix B).

Table 3 shows the main results of the multiparametric fit procedure. In this table the minimum of the ξ^2 function , the contributions to ξ^2_{min} from MACRO data (χ^2_M), the contribution from direct measurements (χ^2_D), the number of degrees of freedom and the ξ^2_{min} per degree of freedom, at different λ_D values are reported. This table shows that MACRO multimuon data and direct measurements are incompatible in the common range of primary energy. The contribution to ξ^2_{min} of the direct measurements ranges from χ^2_D=230 at λ_D =1 to χ^2_D=260 at λ_D = 0.01. We show in Appendix C that at $\lambda_D \sim 0.01$ the ξ^2_{min} roughly reaches its asymptotic limit ($\lambda_D \to 0$) and therefore can be considered as determined by MACRO data alone.

We assume as the best fit of our data the primary cosmic ray composition model obtained from the multi-parametric fit for λ_D=0.01 (hereafter referred to as "standard fit"), of which the basic parameters are summarized in Table 4. The procedure to derive these parameters, as well as their errors and correlation coefficients, is detailed in appendix D. However the composition models arising from the fitting procedure are similar in the

Table 3
Results of the fit at different λ_D values (λ_M=1).

λ_D	ξ^2_{min}	χ^2_M	χ^2_D	D.o.F.=$\nu_M + \lambda_D \cdot \nu_D$	ξ^2_{min}/D.o.F.
1	243	13	230	98	2.48
0.5	128	12.5	231	60.5	2.11
0.1	35	10.9	241	30.5	1.15
0.01	13.6	11	260	24	0.57

Table 4
Composition parameters obtained in the "standard fit". The spectrum of each component is given by equations (5) and (6) in the text. It has to be noted that only $E_{cut}(Fe)$ is actually fitted. The other energy cutoffs are reported for convenience, but are derived from equation (8).

Mass group	K_1 $(m^{-2}s^{-1}sr^{-1}GeV^{\gamma_1-1})$	γ_1	E_{cut} (GeV)	γ_2
H	1.2×10^4	2.67	2.2×10^5	2.78
He	1.3×10^3	2.47	4.4×10^5	3.13
CNO	3.9×10^2	2.42	1.5×10^6	3.58
Mg	4.5×10^2	2.48	2.6×10^6	3.31
Fe	2.4×10^3	2.67	5.6×10^6	2.46

of the different nuclei over a wide energy range (see section 2), while direct experiments measure single nuclei at fixed primary energy in a limited energy region.

4. Primary spectra

Fig. 6 shows the elemental spectra arising from the "standard fit", superimposed to the experimental data of the direct measurements used in the fit. Fig. 7 shows the all-particle spectrum, superimposed to previous experimental data. [8], Akeno [6], Tunka [9], MSU [7], Tibet ASγ [10]. In these figures the bold line gives the central value of the fit, the dashed lines represent the uncertainties on the spectra (one sigma errors) calculated using the covariance matrix of the parameters given by fitting procedure. It can be easily recognized that the spectrum of the fitted model is higher and flatter than the one obtained from direct measurements alone (shown in fig. 7 as a dashed area), exceeding it by an amount ranging from 15 % at E = 10 TeV to 50 % at E = 100 TeV. This fact is responsible of the deficit of the order of at least 25 % in the predicted rates, observed in our previous analysis based on trial composition models [12]. Indeed the models used in our earlier analysis have been tailored to render directly measured elemental abundances at $\lesssim$ 100 TeV

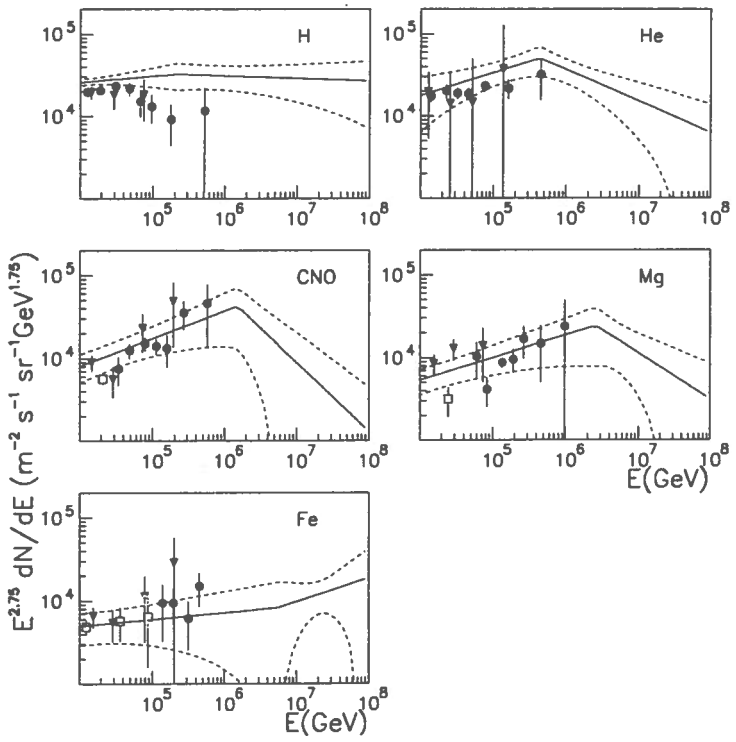

Figure 6. *Elemental spectra arising from the "standard fit", superimposed to the experimental data of the direct measurements used in the fit. Solid lines: central value of the fit, dashed lines: spectra at $\pm 1\sigma$ error, calculated using the covariance matrix of the parameters given by fitting procedure. Symbols for direct measurements same as in fig. 5*

knee. We emphasize that these measurements, shown in fig. 7 for comparison, are not used in the minimized function.

The fitted all-particle can be suitably represented with single power laws at primary energies far from the knee region, with a gradual change at intermediate energies. The corresponding spectral indexes are 2.56±0.05 for E<500 TeV and 2.9±0.3 for E>5000 TeV.

4.1. Sensitivity to the knee

We verified that the rigidity cut hypothesis (8) assumed in the fitting procedure is consistent with our data by making a fit without this assumption. In this fit we fixed all the other parameters, but $E_{cut}(A)$, at the values shown in Table 4 and we fitted independently $E_{cut}(A)$ releasing the relationship (8). The resulting values

$$E_{cut}(H) = 10^{(5.3\pm0.6)}GeV, \quad E_{cut}(He) = 10^{(5.7\pm0.2)}GeV$$

$$E_{cut}(CNO) = 10^{(6.2\pm0.1)}GeV, \quad E_{cut}(Mg) = 10^{(6.5\pm0.1)}GeV$$

$$E_{cut}(Fe) = 10^{(6.8\pm0.5)}GeV$$

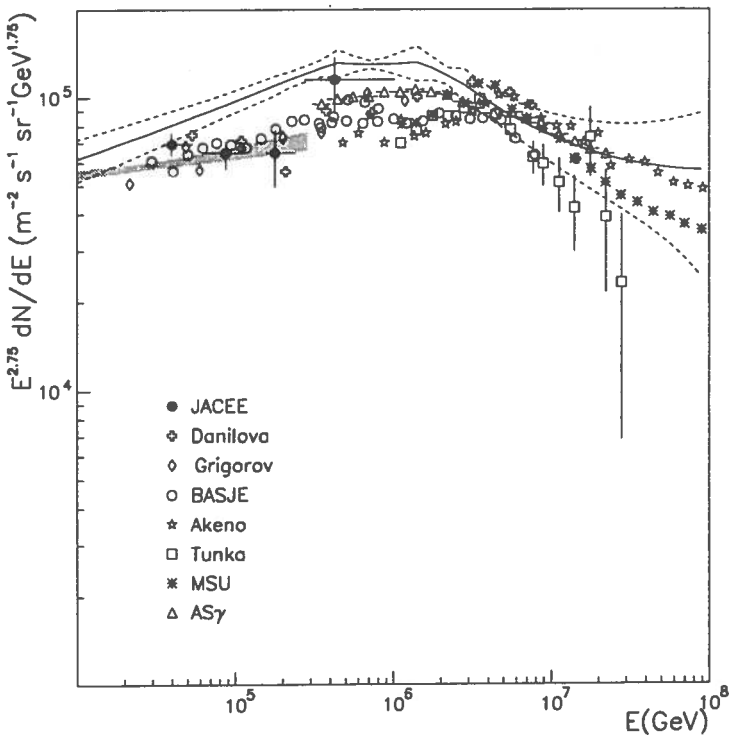

Figure 7. *All-particle spectrum arising from the "standard fit" (solid line: best value; dashed lines: $\pm 1\sigma$ error) superimposed to previous experimental data: JACEE [40], Danilova [5], Grigorov [44], BASJE [8], Akeno [6], Tunka [9], MSU [7], Tibet ASγ [10]. Dashed area: spectrum obtained from the fit of direct measurements shown in fig. 5.*

As shown in fig. 7 the all-particle spectrum arising from the MACRO composition analysis indicates the sensitivity of MACRO data to the knee. To prove this, we have performed a different fit under the assumption of a single power law for each group (corresponding to 10 free parameters). As a result we obtained a probability that ξ^2 exceedes ξ^2_{min} of 5.8 % to be compared with the value of 96 % in the case of the two spectral index hypothesis. This comparison implies that the change of the slope at the knee is preferred from MACRO data. It has to be emphasized that this result emerges directly from multimuon data, since, as reported in section 3.2, single slope spectra give a good description of the data of direct measurements. This is a remarkable outcome of this analysis since for the first time an underground experiment shows sensitivity to the knee.

4.2. Best fit procedure on the muon rate ratios

In the fitting procedure described in the previous sections we used the absolute multiple muon rate measurements of the individual multiplicities. As reported in sections 2.2 and refsec:muonp the uncertainties on Monte Carlo predictions from the knowledge of the cosmic ray flux, MACRO and muon propagation through the rock affect the absolute

uncertainties. We therefore applied the multi-parametric fit procedure to the muon rate ratios $r(N_\mu)=R(N_\mu)/R(1)$, defining χ^2_M, in equation (7), with $r(N_\mu)$ in place of $R(N_\mu)$. In this way only the shape of the multiplicity distribution is taken into account, while the absolute normalization of the primary fluxes is fixed by the data of the direct measurements. The all-particle spectrum arising from the fit of the rate ratios for $\lambda_D = 0.01$, is shown in fig. 8. This spectrum has the same shape of the spectrum obtained from the fit of the absolute rates, shown in fig. 7 and, as expected, is in better agreement with the absolute normalization of the direct measurements. However, at higher energies, the spectrum shown in fig. 8 is less consistent with the EAS measurements with respect to the one obtained from the fit of the absolute rates.

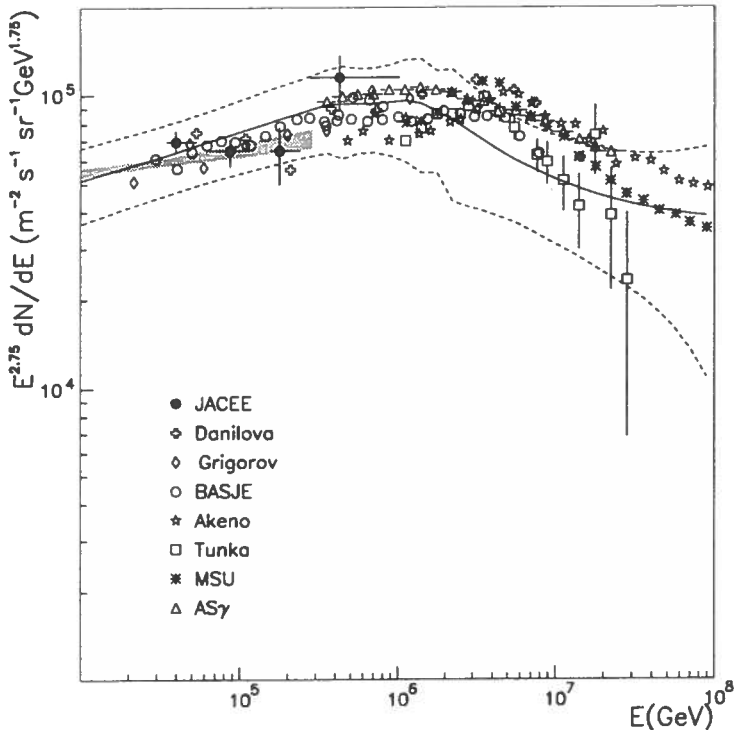

Figure 8. *All-particle spectrum arising from the fit of of the rate ratios $r(N_\mu)=R(N_\mu)/R(1)$, superimposed to previous experimental data. Dashed area: spectrum obtained from the fit of direct measurements.*

5. Primary composition

Fig. 9 shows the dependence of the average mass number of cosmic rays $< A >$ on primary energy. The dependence on primary energy of the relative abundances of the light (H+He), medium-heavy (CNO+Mg) and very-heavy (Fe) components of the fitted

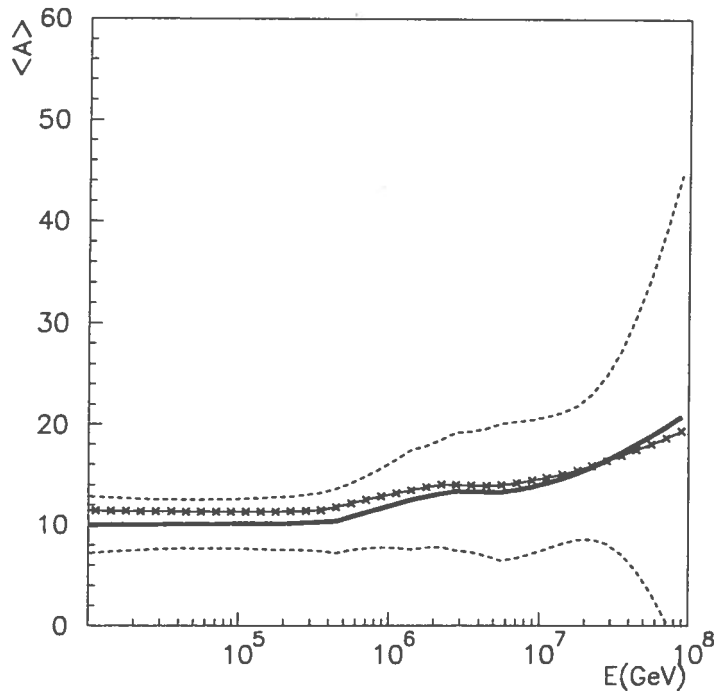

Figure 9. *Dependence of the average mass of cosmic rays on primary energy. Solid line:* $< A >$ *arising from the "standard fit", chain line:* $< A >$ *arising from the fit of the rate ratios.*

one to each other, in terms of $< A >$ and relative abundances of mass groups. This gives us confidence in the reliability of the present analysis of primary composition. Table5 shows at different primary energies the relative abundances of each elemental group as estimated in the "standard fit".

Both $< A >$ and the relative abundances show a weak dependence on the primary energy below 10^6 GeV. Even within large uncertainties our data show that the composition changes at the knee and support a moderate increase of the average mass number at higher energies.

In fig. 11, $< A >$ obtained in our "standard fit" is compared with other measurements and predictions. In particular, fig. 11a shows that our $< A >$ estimate is consistent, within errors, with the ones obtained from the fit of direct measurements (shown as dashed area in the figure) and from other composition analyses of direct observations [40][41] and EAS array data [45][46], in the same primary energy region. In this figure $< A >$ is displayed up to $\sim 10^{18}$ eV, exceeding the region covered by MACRO by more than one decade, in order to include the composition results from Fly's Eye [47] in the EeV region. The dash-dotted line gives the $< A >$ dependence on primary energy arising from a two component fit of the ratio *iron flux/proton flux* as obtained from Fly's Eye elongation data between $10^{17.5}$ and $10^{19.5}$ eV. A three component analysis, with the insertion of a CNO component and fixing the Fe contribution to 40%, gives the point represented with a star

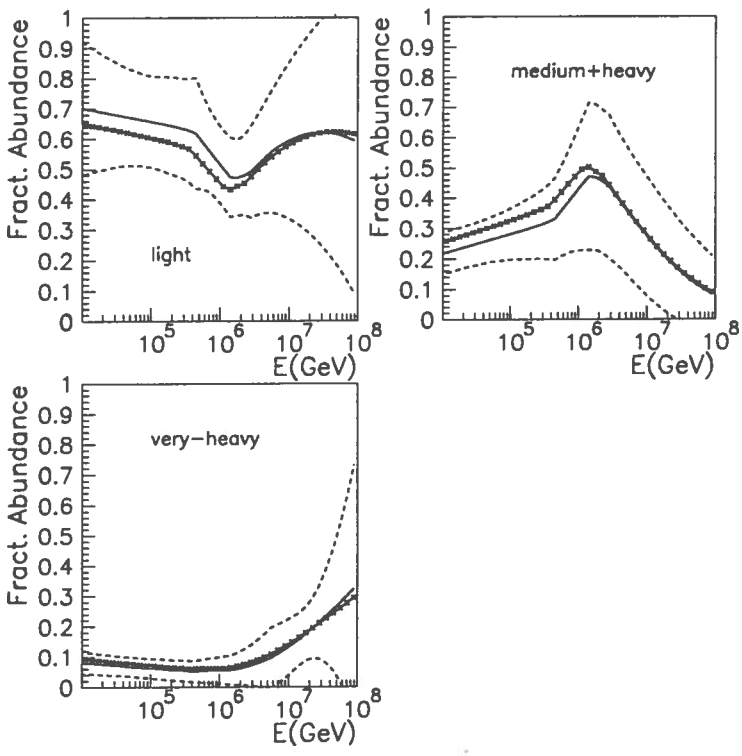

Figure 10. *Dependence on primary energy of the relative abundances of the light (H+He), medium-heavy (CNO+Mg) and very-heavy (Fe) components. Line types same as in fig.9.*

mass composition (CMC) model [15]; the Σ model [16], which is a fit of direct measurements, to be considered limitedly to primary energies below the knee; a recent model proposed by Swordy [48] in the context of a simple leaky box model, incorporating a cutoff propagation pathlength to account for the unobserved anisotropy at high energies. This comparison confirms that MACRO data exclude a primary composition that becomes heavier with increasing energy, as dramatically as does the Heavy model. Nevertheless the achieved resolution prevents from discriminating among different models that, though originating from different physical hypotheses, are characterized by a flat or slowly increasing $< A >$ as a function of the primary energy.

6. Composition dependence of other muon features

When dealing with indirect measurements of primary cosmic ray composition, it is important to identify as many experimental observables as possible which can help in the validation of the composition models. In order to test the fitted composition model, the MACRO experimental results on vertical muon intensity and decoherence function have been compared with the predictions of this model.

Table 5
Relative abundances of the different elemental groups in the "standard fit".

E (TeV)	H	He	CNO	Mg	Fe
10	0.42±0.08	0.28±0.19	0.13±0.06	0.09±0.03	0.08±0.04
10^2	0.31±0.09	0.34±0.11	0.18±0.07	0.11±0.04	0.06±0.03
10^3	0.23±0.08	0.29±0.09	0.29±0.17	0.14±0.08	0.05±0.04
10^4	0.35±0.17	0.21±0.14	0.16±0.15	0.16±0.11	0.12±0.08

of depth agrees with the world average within a few percent, so that the comparison between our data and the results of a Monte Carlo simulation confirms our understanding of detector acceptance and overburden systematics. Fig. 12 shows that two extreme models, as the Heavy and Light [14] ones, which are based on direct measurements as starting points for extrapolation to higher energies, are inconsistent with the experimental behaviour of the depth intensity curve. Assuming the MACRO composition model derived from the "standard fit", we obtain a good agreement between the predictions of the Monte Carlo simulation and the experimental data, both in absolute normalization and slope. This scenario is a further confirmation of the results of our previous analysis on trial models [12, 11, 13].

6.2. The decoherence curve

The shape of the separation distribution of muon pairs measured by MACRO has been demonstrated to be sensitive to hadronic interaction models, and has allowed a validation of the HEMAS interaction model [21, 22]. A limited dependence on the composition model is also shown in these references. In fig. 13 we plot the measured decoherence distribution compared to the prediction from different composition models. Simulated events have been generated, using the HEMAS hadronic interaction model, according to different composition models: the Light and Heavy models [14] and the model arising from the MACRO "standard fit". Here each multiple muon event having N_{pair} unambiguously reconstructed pairs has unit weight, *i.e.* each pair enters with a weight $1/N_{pair}$ and the different distributions are normalized one to the other in order to emphasize the comparison of shape. We notice that the "standard fit" model provides also the best agreement to the shape of the decoherence distribution in space. This is significant, since we do not use the muon separation data in the fit.

However, we note that also the normalization of the decoherence curve is of interest, since it introduces additional sensitivity to the spectrum and composition of primary cosmic rays. The primary composition has different effects on the muon flux and decoherence curve normalization. The inclusive muon flux tends to be dominated by the proton part of the primary composition, while other nuclei, if present, give large contributions to the decoherence curve [24]. This is due to the fact that in the decoherence curve a single event of high multiplicity multiplicity N_μ weights heavily by producing $N_\mu(N_\mu - 1)/2$ pairs. Therefore the decoherence function receives a large contribution from the richest bundles and then is dominated by the contribution of the heavy primary nuclei, reflecting

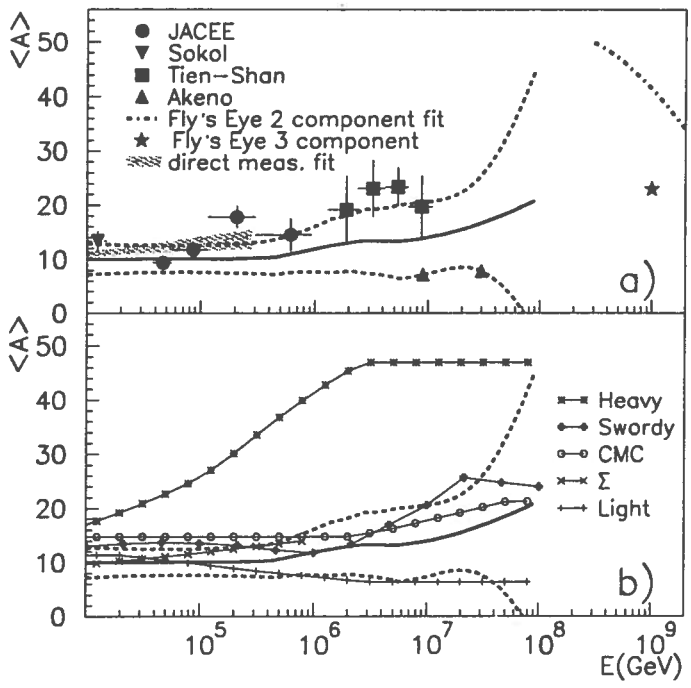

Figure 11. *Comparison of the average primary mass arising from our "standard fit" (solid line: central value; dashed line: value at one sigma error) with other measurements a) and predictions b). References are given in the text.*

can be performed without bias by MACRO only by considering the muon separation projected in one view. In fig. 14 the MACRO experimental muon lateral separation projected in the wire view is shown superimposed to Monte Carlo predictions, for events with any multiplicity. The different normalization of the distributions obtained with the two "extreme" models, in conjunction with the shape analysis described above, show sensitivity of the muon lateral distribution tc primary composition. The prediction of the Light model is in disagreement with the experimental data. The normalizations of the Heavy and the "standard fit" models are in good agreement with the experimental data, apart from the shape consideration derived from fig. 13. Enhanced sensitivity to primary composition is achieved from the study of the same distribution as a function of the multiplicity. In fig. 15 the comparison between experimental and Monte Carlo distributions for events with multiplicities N_μ=2, N_μ=3, N_μ=4÷6 and N_μ=7÷20 is shown. From these comparisons one can extract interesting information. For low multiplicity events the predictions of the two "extreme" models are very similar, while the sensitivity to primary composition increases at higher multiplicities. The Light model, which contains a very small fraction of heavy nuclei, underestimates the rate of muon pairs in the whole separation range, independent of the event multiplicity. On the contrary the Heavy model, which contains a large fraction of heavy nuclei, has a different behaviour. The predictions

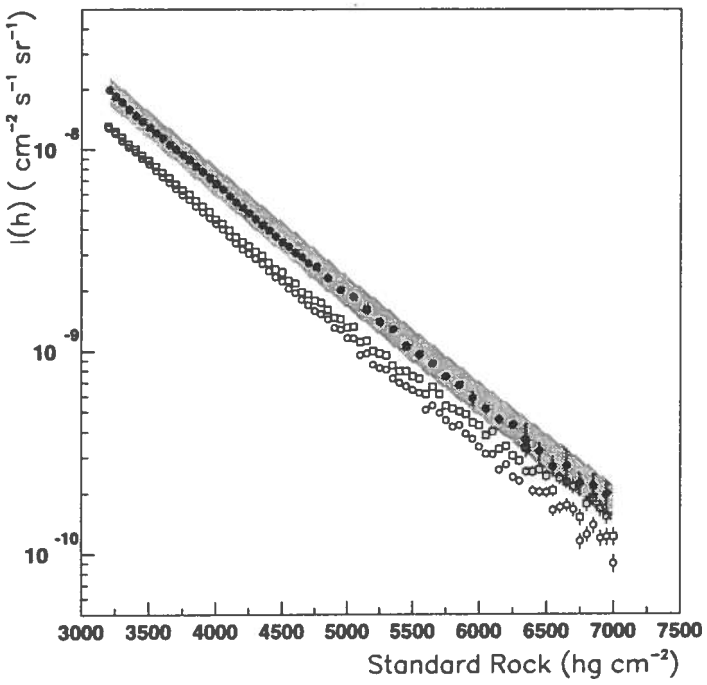

Figure 12. *MACRO vertical depth intensity data points, compared with the results of Monte Carlo simulations. Full circles: experimental data; open squares: Light model; open circles: Heavy model; dashed area: "standard fit" model within $\pm 1\sigma$ errors on the fitted parameters.*

agreement with experimental data for higher separations. For multiplicities N_μ=4÷6 the Heavy model agrees with experimental data in the whole separation range. Increasing the multiplicity (N_μ=7÷20), the Heavy model overestimates the experimental rates, clearly indicating that this model contains an excess of heavy nuclei with respect to the real content of these nuclei in the primary cosmic rays. We also notice that at high multiplicity the shapes predicted by the Light and Heavy model are different from the measured ones. The MACRO "standard fit" model reproduces the lateral distribution of experimental data in the whole multiplicity range both in shape and normalization. This is an important result of this analysis, since it shows that the composition estimated from muon rates only is consistent also with higher order features of multimuon events.

7. Discussion

In section 2 we have discussed in detail the contributions to the predictions of multimuon rates coming from different sources of systematic uncertainties present in our simulation: uncertainties in the hadronic interaction model, in the knowledge of the map of the rock around MACRO, and in muon propagation through the rock. The uncertainties from the knowledge of the rock around MACRO and the muon propagation through

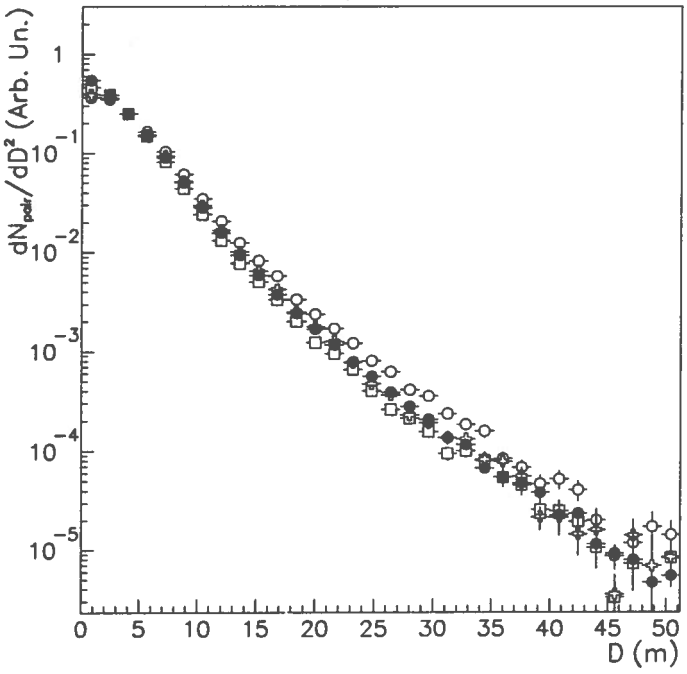

Figure 13. *Comparison between experimental and predicted muon lateral separations for events with any multiplicity. Full circles: experimental data; open squares: Light model; open circles: Heavy model; open crosses: "standard fit" model.*

dependence on energy). Therefore the main contribution to systematic uncertainties in our Monte Carlo simulation is due to the hadronic interaction model that could eventually act differently in the various energy regions. In section 2.1 this effect is estimated to be of the order of about 10% in the predicted multimuon rates. In order to study the dependence of our results from the best fit procedure on the adopted hadronic interaction model, we applied the multi-parametric fit procedure using the SIBYLL code as hadronic interaction model. The predicted multimuon rates (3) have been fitted using probabilities $D_A(E, N_\mu)$ calculated with SIBYLL on a reduced sample of simulated events, in place of those calculated with HEMAS. The all-particle spectrum arising from the fitting procedure assuming the SIBYLL model is at most of the order of 10 % lower than the one shown in fig. 7, obtained with HEMAS. This value can be considered as an estimate of the systematic uncertainty in our fitting procedure. Nevertheless the results from the fit using the SIBYLL model are very similar to the corresponding ones with HEMAS, in terms of $< A >$ and relative abundances of mass groups.

Important sources of uncertainties in the hadronic interaction model (HEMAS, SIBYLL and in general any other model) come from our limited knowledge of proton air and nucleus-air inclusive meson production at very high energies. A model for hadronic and nuclear interactions to be used in cosmic ray physics should work from the pion produc-

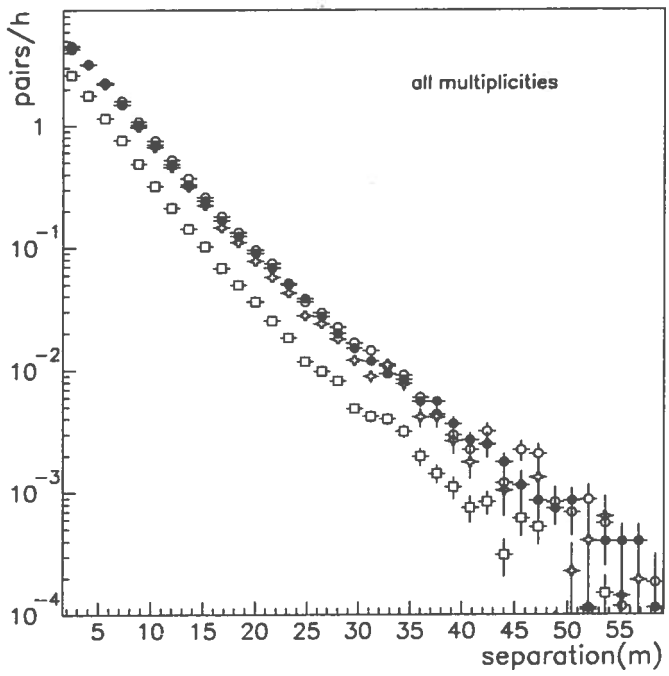

Figure 14. *Comparison between experimental and predicted muon lateral separations projected in the wire view for events with any multiplicity. Same symbols as in fig.13. Projected separations lower than 1 m have not been considered because of experimental inefficiencies in the close track separation.*

proton energy $E_p \sim 1000$ TeV. However, in the highest energy part of the energy region investigated in this search, which corresponds to centre of mass energies $\sqrt{s} \approx 10$ TeV (i.e. LHC energies or greater) no direct collider measurements are yet available, and lower energy data must be extrapolated. Nucleus-nucleus data from accelerator experiments need a much stronger extrapolation. This situation could lead to the belief that possible inadequacies of interaction models, that are tailored to experimental data, are increasing with energy, but are virtually absent in the energy region below the knee. Indeed our results obtained from the "standard fit" show the strongest discrepancies with existing cosmic ray data just in that region.

For the relevant kinematical region accessed (e.g., the Feynman-x interval), there are important differences between cosmic ray cascades and particle production at accelerators. At colliders, the central region in hadron-hadron collisions is usually best measured. At lower energies, in fixed target experiments, the forward fragmentation region is more easily accessible, yet very little data are available at x_F exceeding 0.1. Multiple muons observed in underground detectors come from different kinematical regions determined by the energy of primaries that produce the muons. In particular one can see that multimuon events originating from less energetic primaries are preferentially produced from parents in the very forward fragmentation region, whereas at higher primary energies

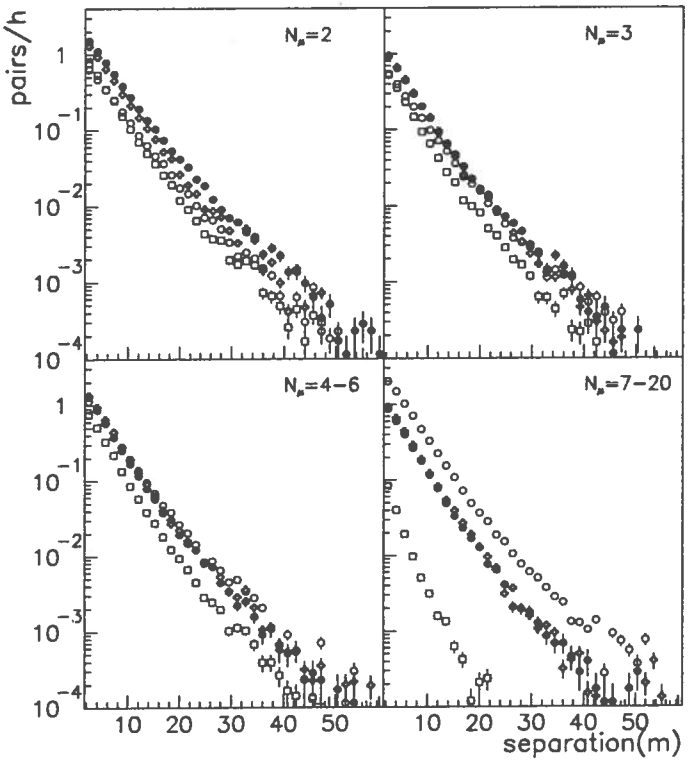

Figure 15. *Comparison between the experimental muon lateral separation projected in the wire view as a function of the event multiplicity. Same symbols as in fig.13.*

it can be recognized that the highest x_F parents are the main contributors of the low multiplicity muon events and then largely determine the inclusive muon rates. Therefore possible inadequacies of the hadronic interaction models in the far fragmentation region could, at least partly, explain the discrepancies between multimuon results and direct measurements.

8. Concluding remarks

The multi-parametric fit of muon rates is a successful tool for studying the primary cosmic ray composition. We showed that multimuon data require the contribution of all the elemental groups in order to explain the observed muon rates in a wide multiplicity range. An important outcome of our fitting procedure is that MACRO data show sensitivity to the energy steepening above the knee.

The fitted all-particle spectrum shows a good consistency with EAS array measurements whereas, in the lower energy region, it is higher by ~10% at 10 TeV to ~50% at 100 TeV with respect to direct measurements in the same interval. The spectral indexes of the fitted energy spectrum are 2.56±0.05 for E<500 TeV and 2.9±0.3 for E>5000 TeV with

Table 6
Average x_F of the parent of the muons at MACRO depth, in different ranges of primary energy. Events generated using the HEMAS interaction model.

E (TeV)	N_μ=1	N_μ=2÷4	$N_\mu \geq 5$
<10	0.41	0.34	
$10 \div 10^2$	0.25	0.19	0.09
$10^2 \div 10^3$	0.23	0.19	0.16
$10^3 \div 10^4$	0.22	0.20	0.18
$10^4 \div 10^5$	0.20	0.20	0.19

a weak dependence on the primary energy below about 1000 TeV. Even within larger uncertainties our data support a moderate increase of the average mass number at higher energies.

The analysis presented in this paper actually depends on the adopted hadronic interaction model (HEMAS). A comparison with a more recent model, SIBYLL, based on different physical assumptions, leads to spectra differing of the order of 10%, but with a very similar composition.

A. ξ^2 minimization

The estimate of the elemental flux parameters has been performed through a minimization of the function ξ^2 (see equation (9)), in which these parameters appear in two distinct terms:

1. a χ^2 term (χ^2_M) based upon muon multiplicity rates from MACRO data (7). This term includes the flux parameters in the convolution integral (3);

2. a χ^2 term (χ^2_D) built up with direct measurements of individual spectra (10).

The two pieces are used to define the minimized ξ^2 function through a linear combination, with fixed (i.e. not estimated) weight parameters. However the two contributions have a quite different role in our best fit procedure. The first is the primary term from which we want to estimate our parameters and then the corresponding weight ($\lambda_M = 1$) is not changed during the fit process. The second term has the role of constraining the flux parameters to a limited region of the parameter space and therefore the corresponding weight (λ_D) is changed. It is straightforward that setting λ_D to 0 is equivalent to a best fit of MACRO data alone.

The adopted procedure of constraining the flux parameters with external measurements has been suggested by the following considerations:

- the high number of free parameters and the dependence of the muon rates on the composition parameters, through a convolution of primary spectra over a wide ener-

- The application of limits on parameters could in principle solve the previous problem and then prevent the parameters from taking on unphysical values. The minimization with limited parameters is generally (e.g. in MINUIT [38]) achieved with a non-linear transformation of the parameters themselves and unavoidably introduces additional numerical difficulties to the process. Then the success of such minimization strongly depends on the minimized function and, in any case, it is recommended to release the boundary conditions after the minimum is reached, in order to get a reliable calculation of the covariance matrix. In our case this procedure turned out to be unsuccessful, mainly because of numerical problems arising from the intrinsically strong correlations among the parameters in the two-power law function. Furthermore the functional form of elemental spectra prevents an appropriate definition of the parameters boundaries. As a result, minimizations performed using MACRO data alone ($\xi^2 = \chi^2_M$) with limited parameters gave us spectra in reasonable agreement with the ones obtained with the constrained fit, but with parameter errors unreliable on account of unsolved numerical inaccuracies (e.g. covariance matrix not positive-definite).

- The minimization process at decreasing values of λ_D showed a limiting minimum of ξ^2 at a value of λ_D for which the minimization is still good and the evaluation of the covariance matrix is accurate (see appendix C).

Particular care has been taken in order to render the calculation of the ξ^2 function as free as possible of numerical inaccuracies. In our analysis, depending on the actual representation of the elemental fluxes (5),(6), the ξ^2 calculation can be affected by rounding-off errors due to the finite word length in the computer analysis. In particular, the result of the minimization process strongly depends on the energy scale which is used therein. The standard scale that is used in UHE C.R. literature, with primary energy in GeV, is inappropriate for our calculation. In fact our multimuon rates are sensitive to primary energies above a few 10 TeV and the expected spectra rapidly fall off with energy. An energy scale of 10 TeV or more is also to be preferred in order to avoid powers of too high energy values. We found that a scale between a few TeV and a few ten TeV is preferred in our fit; our final choice was an energy unit of 10 TeV. We also redefined the flux parameters in order to render them all of the same size. The spectral indices ($\gamma_1(A)$ and $\gamma_2(A)$) are expected to be of the order of few units and therefore we applied modifications to the other parameters to have them in the same range. This choice produces a covariance matrix calculated with good numerical accuracy. The spectra used in our minimization have the form:

$$\Phi_A(E) = 10^{-3}\kappa_1(A) \quad \times(E/10\ TeV)^{-\gamma_1(A)} \quad \text{for } E < 10^{A_{cut}(A)+1}\ TeV \tag{11}$$

$\kappa_1(A)$, $\gamma_1(A)$, $\gamma_2(A)$ and $\Lambda_{cut}(A)$ are the parameters that are actually estimated. The new parameters are related to the ones in (5),(6) as follows:

$$K_1(A) = 10^{-3}\kappa_1(A) \times (10\ TeV)^{\gamma_1(A)} \tag{13}$$

$$E_{cut}(A) = 10^{\Lambda_{cut}(A)} \times (10\ TeV). \tag{14}$$

B. ξ^2 function

The ξ^2 function defined in (9) is not properly a χ^2 variable as it results from a linear combination of two distinct χ^2 components. We calculated the probability distribution of such variable as:

$$p(\xi^2) = \int_0^{\xi^2/\lambda_M} \mathcal{P}_{\nu_M}(\chi^2_M)\frac{1}{\lambda_D}\mathcal{P}_{\nu_D}(\frac{\xi^2 - \lambda_M\chi^2_M}{\lambda_D})d\chi^2_M \tag{15}$$

where $\mathcal{P}_\nu(\chi^2)$ is the probability of χ^2 with ν degrees of freedom. In fig. 16 we show the cumulative probabilities:

$$P(\geq \xi^2) = \int_{\xi^2}^{\infty} p(z)dz \tag{16}$$

as obtained from (15), in the range of λ_M and λ_D we actually used in our fit (λ_M =1 and $\lambda_D = 1 \div 0.01$). It can be easily recognized that, in this range, our cumulative probabilities are very close to, and in some cases indistinguishable from, the cumulative χ^2 probability with $\lambda_M\nu_M + \lambda_D\nu_D$ degrees of freedom (dashed curves):

$$P(\geq \xi^2) \approx \int_{\xi^2}^{\infty} \mathcal{P}_{\lambda_M\nu_M+\lambda_D\nu_D}(\chi^2)d\chi^2. \tag{17}$$

This means that, in the range of weight parameters considered in our fit, ξ^2 behaves as a χ^2 variable with a number of degrees of freedom (D.o.F.) given by:

$$\nu = \lambda_M\nu_M + \lambda_D\nu_D. \tag{18}$$

C. ξ^2_{min} as a function of λ_D

In appendix A we described the procedure we used to estimate the flux parameters through a constrained fit of MACRO multimuon data. For each value of λ_D (≤ 1) a minimum of the ξ^2 function has been calculated using the MINUIT minimization package. The minimization turns out to be successful up to very low values of λ_D, but numerical problems, mainly in the calculation of the covariance matrix, prevent from obtaining reliable parameters and errors for λ_D <0.01. Fig. 17 shows the values of ξ^2_{min} (solid circles) reached at different values of λ_D. A solid line shows the corresponding number of degrees of freedom calculated according to equation (18). It is evident from this figure that ξ^2_{min} has an asymptotic behaviour with λ_D and reaches a minimum value already

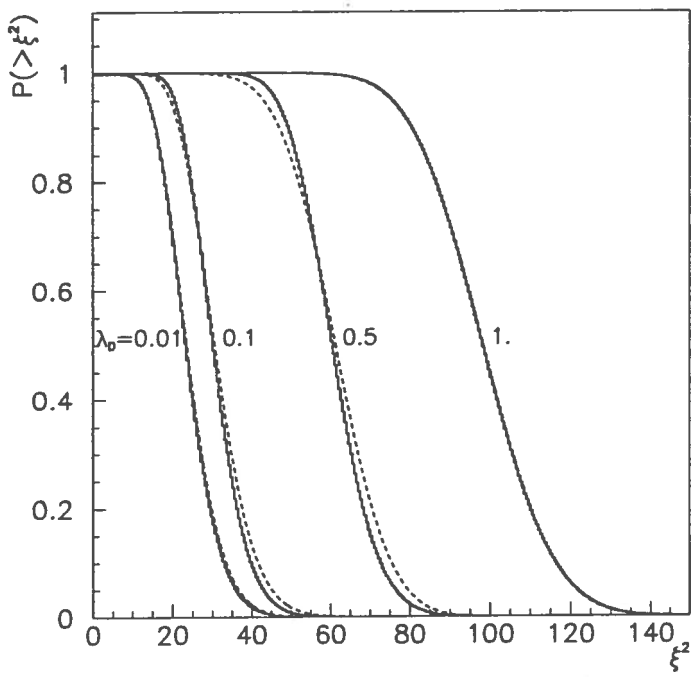

Figure 16. *Cumulative probability distributions $P(\geq \xi^2)$ (equation (15), in the text) for different values of λ_D (solid histograms). For comparison, dashed lines show the cumulative χ^2 probabilities for $\lambda_M \nu_M + \lambda_D \nu_D$ degrees of freedom.*

unsolvable numerical problems. On the other hand, the best fit parameters show a very weak dependence on λ_D and, in particular, the global results (e.g. the all-particle spectrum and the average primary mass as a function of primary energy) are roughly independent from it. This can be seen in fig. 18 where the average mass is plotted against primary energy at various values of λ_D. This fact gives us confidence in the estimate of the flux parameters and points out the high potential of multimuon data in the determination of the primary composition.

The actual value of the limiting minimum of ξ^2 (ξ^2_{min}=13.6), which appears to be somewhat lower than the "equivalent" number of degrees of freedom (ν=24, as given by (18)), requires additional discussion. The corresponding confidence level turns out to be $\sim$ 95 % and could suggest an overestimate of the error in the multimuon rates at the various multiplicities (see equation (7)). The various sources of experimental errors on muon rates are discussed in [17]. These include errors from muon reconstruction (formula (4) in [17]), unfolding errors in the high multiplicity region and systematic errors to account for the uncertainties in the merging of the reconstructed data sample with the scanned one. Apart from muon multiplicities ≤ 15, where $\sigma[R^{meas}(N_\mu)]$ is roughly equal to the statistical error (i.e. $\sigma[R^{meas}(N_\mu)]/R^{meas}(N_\mu) \sim 1/\sqrt{(R^{meas}(N_\mu))}$, at higher multiplicities both the systematic errors and the unfolding errors are rather large and

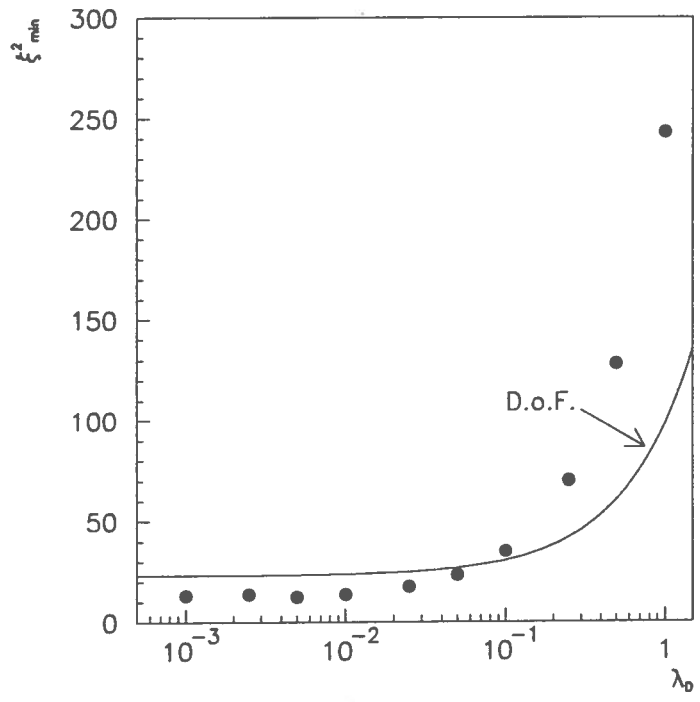

Figure 17. ξ^2_{min} *(solid circles) as a function of the weight parameter* λ_D. *The solid curve shows the number of degrees of freedom calculated according to equation (16), in the text).*

we recall that also the errors on predicted rates (see equation (7)) are roughly of the same order as the experimental ones. This is due to the impossibility of increasing the size of the simulated data sample on account of the extremely long CPU time required in the event generation (see section 2).

D. Best fit parameters and errors

In the previous section of this Appendix, we showed that the constrained fit reaches an asymptotic value of ξ^2_{min} at $\lambda_D \leq 0.01$. In section 3.2 we give our results at $\lambda_D = 0.01$ for which the convergence of the minimization process is reached without problem and the covariance matrix is still accurate. The best fit parameters obtained at this λ_D value, for the case of χ^2_M built up with the absolute muon rates R(N_μ), ("standard fit") are shown in Table 4, in the usual UHE C.R. energy scale (GeV). Parameter errors are not given in that table, since they are meaningless at such a scale, so different from the one actually used in our fit (see appendix A), because of the strong correlations among parameters. Table 7 shows the best fit parameters obtained in the "standard fit", from which the values reported in Table 4 are derived. As it can be easily recognized, both the energy scale and the redefinition of the parameters render the minimization free of possible numerical inaccuracies, being the best fit parameters roughly of the same size.

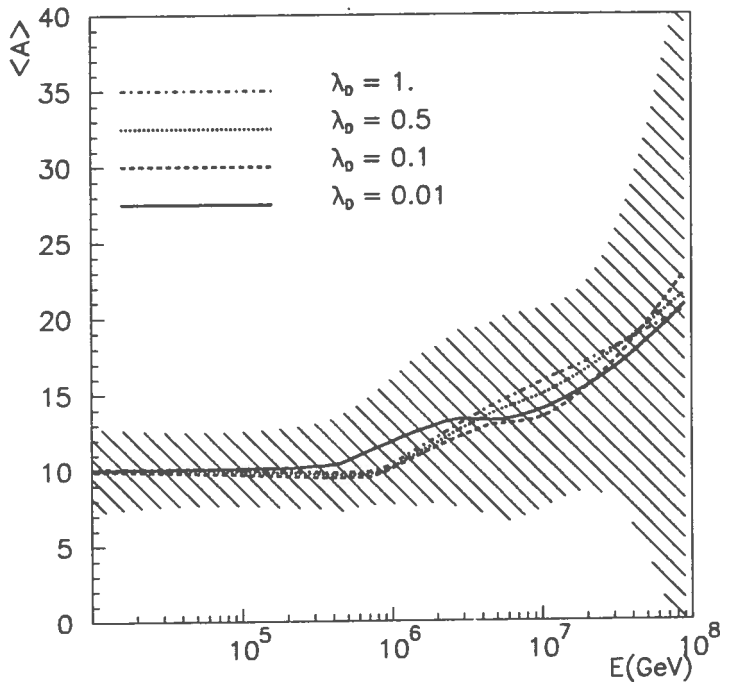

Figure 18. *Average mass as a function of primary energy at different values of the direct measurement weight parameter (λ_D). The hatched area gives <A> within $\pm 1\sigma$ error for λ_D =0.01.*

of the correlation matrix are shown.

E. Consistency check of the minimization procedure

In order to check our minimization procedure, we tried to reconstruct *a priori* known primary cosmic ray compositions. For this purpose events generated using specific test composition models have been processed through the same multi-parametric fit procedure as experimental data and the fitted spectra have been compared with the input ones. Fig. 19 shows the result for one of these checks when the test composition model is a constant mass composition with rigidity dependent cutoff. The elemental spectra are determined by only 8 parameters: 5 normalization factors $K_1(A)$, two spectral indexes γ_1 and γ_2, equal for each group, and one energy cutoff. This case is of particular interest for demonstrating the sensitivity of MACRO data to composition, since it allows us to perform the minimization of the χ^2_M term alone (i.e. setting λ_D=0 in equation (9)), without the need of the constraining term $\lambda_D \cdot \chi^2_D$ and the consequent extrapolation procedure described in appendix C. It is important to point out that the comparison between input spectra and fitted ones has to be done on their energy dependence and not comparing individual parameters. Each estimated parameter is expected to agree with the corresponding input parameter within $\pm 1\sigma$, at 68% C.L., *when all the others have any*

Table 7
Best fit parameters as obtained in the "standard fit" ($R(N_\mu)$, $\lambda_D = 0.01$). κ_1 parameters are expressed in $m^{-2}s^{-1}sr^{-1}(10\ TeV)^{-1}$.

No.	Type	best fit value
1	γ_1(H)	2.67 ± .13
2	γ_1(He)	2.47 ± .21
3	γ_1(CNO)	2.42 ± .15
4	γ_1(Mg)	2.48 ± .12
5	γ_1(Fe)	2.67 ± .16
6	γ_2(H)	2.78 ± .13
7	γ_2(He)	3.13 ± .26
8	γ_2(CNO)	3.58 ± .53
9	γ_2(Mg)	3.31 ± .53
10	γ_2(Fe)	2.46 ± .72
11	κ_1(H)	2.55 ± .24
12	κ_1(He)	1.7 ± 1.1
13	κ_1(CNO)	.81 ± .31
14	κ_1(Mg)	.53 ± .18
15	κ_1(Fe)	.50 ± .21
16	Λ_{cut}(Fe)	2.75 ± .26

Table 8
Non-diagonal correlation matrix elements as obtained in the "standard fit". The correspondence between parameter number and type is given in table 7.

No.	1	2	3	4	5	6	7	8	9	10	11	12	13	14	
2	-.37														
3	.33	-.42													
4	-.01	.01	-.02												
5	.00	-.06	.14	.00											
6	-.41	-.02	-.03	-.09	-.34										
7	.45	-.38	.42	.05	.01	-.22									
8	-.21	.17	.12	.03	-.37	.32	-.17								
9	.09	-.16	.40	-.43	-.24	.19	.33	.03							
10	.02	.09	-.31	.02	-.84	.23	-.08	.15	.08						
11	.39	-.93	.24	.03	.03	-.06	.27	-.12	.05	-.03					
12	.08	.87	-.18	.00	-.03	-.19	-.12	.08	-.06	.04	-.87				
13	-.02	.10	.43	.00	-.01	-.01	-.07	-.01	-.03	.03	-.07	.03			
14	.00	.03	.00	.22	-.01	,03	-.04	-.03	.13	.01	-.03	.01	.00		
15	.01	.01	-.03	.01	.13	.11	.00	.12	.07	.26	-.01	.01	.00	.00	
16	.17	-.32	.70	.39	.17	.03	.53	.29	.20	-.38	.18	-.13	-.06	-.14	-.

the fitting procedure and the input spectra (fig. 19) confirms the ability of the multi-parametric fit procedure to reconstruct the primary energy spectra.

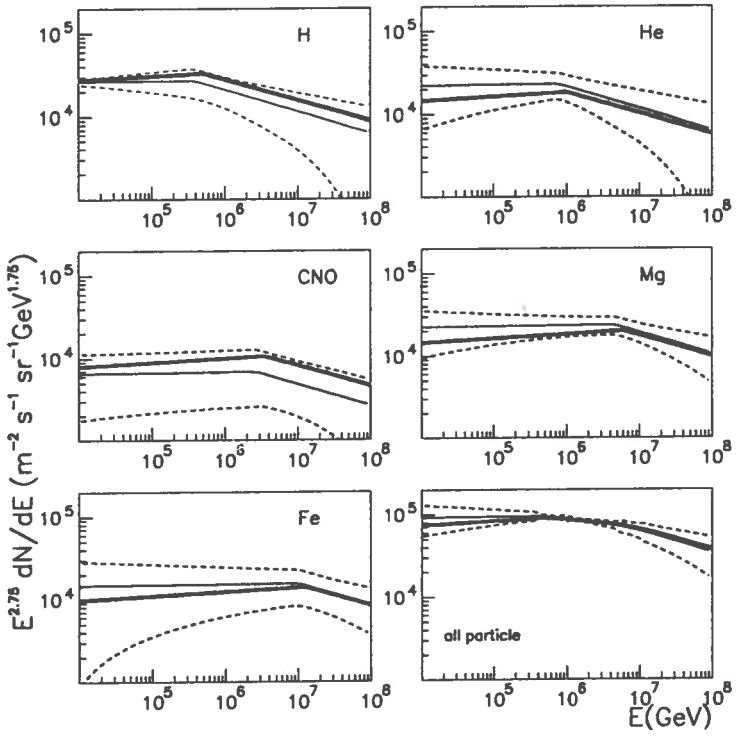

Figure 19. *Input spectra (bold line) and reconstructed spectra for a constant mass composition model with spectral indexes γ_1=2.7 and γ_2=3 and a rigidity cutoff of 500 TV.*

Acknowledgments

We would like to thank F. James, D. Drijard and E. Di Capua for suggestions given in the function minimization and error handling. We also thank T.K. Gaisser and T. Stanev for many useful discussions about hadronic interaction models.

REFERENCES

1. P.O. Lagage and C.J. Cesarsky, *Astronom. Astrophys.* **125** (1983) 249
2. For a review of acceleration mechanisms and diffusive propagation see for example, T.K. Gaisser, Cosmic Rays and Particle Physics, Cambridge University Press, cambridge, England.
3. H.J. Völk and P.L. Biermann, *Ap. J. Lett.* **333** (1988) L65
4. G.V. Kulikov and G.B. Khristiansen, *Sov. Phys. JETP* **35** (1958) 635
5. T.V. Danilova et al., *Proc. of 15th Int. Cosmic Ray Conf., Plovdiv*, **8** (1977) 129
6. M. Nagano et al., *J. Phys. G: Nucl. Part. Phys.* **10** (1984) 1295
7. Yu. Fomin et al., *Proc. of 22nd Int. Cosmic Ray Conf., Dublin*, **2** (1991) 85
8. BASJE Collaboration, H. Yoshii et al., *Proc. of 24th Int. Cosmic Ray Conf., Rome*, **2** (1995) 703; Y. Shirasaki , *Master Thesis* (1994)
9. S.V. Bryanski et al., *Proc. of 24th Int. Cosmic Ray Conf., Rome*, **2** (1995) 724
10. Tibet ASγ Collaboration, M. Amenomori et al., *Proc. of 24th Int. Cosmic Ray Conf., Rome*, **2** (1995) 736; ICRR-Report-349-95-15 (1995) submitted to *Ap. J.*
11. The MACRO Collaboration (S. P. Ahlen et al.), *Phys. Rev. D* **46** (1992) 895.
12. The MACRO Collaboration (S.P. Ahlen et al.), *Proc. 23rd Int. Cosmic Ray Conf., Calgary,* **2** (1993) 97.
13. The MACRO Collaboration (S. P. Ahlen et al.), *Underground muon physics at MACRO*, LNGS - 94/114, (1994).
14. G. Auriemma et al., *Proc. 21st Int. Cosmic Ray Conf., Adelaide,* **9** (1990) 362.
15. J. Kempa and J. Wdowczyk, *J. Phys. G: Nucl. Part. Phys.*, **9** (1983) 1271.
16. EASTOP and MACRO Collaborations (M. Aglietta et al.), *Phys. Lett.* **B337** (1994) 376.
17. The MACRO Collaboration (S. P. Ahlen et al.), previous article in this issue.
18. R. Brun et al., CERN Publication DD/EE/84-1 (1992).
19. C. Forti *et al.*, *Phys. Rev. D* **42** (1990) 3668.
20. G.J. Alner *et al.*, *Physics Letters* **167B** (1986) 476.
21. The MACRO Collaboration (S. P. Ahlen et al.), *Phys. Rev. D* **46** (1992) 4863.
22. The MACRO Collaboration (S. P. Ahlen et al.), *Proc. 23rd Int. Cosmic Ray Conf., Calgary,* **2** (1993) 93.
23. J. Engel et al., *Proc. 22nd Int. Cosmic Ray Conf., Dublin,* **4** (1991) 1.
24. J.W. Elbert, T.K. Gaisser and T. Stanev, *Phys. Rev. D* **27** (1983) 1448.
25. G. Battistoni et al., LNF-95/038(P) (1995) submitted to *Astroparticle Phys.*
26. G. Battistoni, C. Forti and J. Ranft, *Astroparticle Phys.*, **3** (1995) 157
27. R. S. Fletcher et al., *Phys. Rev. D* **50** (1994) 5710.
28. See for instance A. Capella et al., *Phys. Rev. Lett.* **58** (1987) 2015, and references therein.
29. T. K. Gaisser and T. Stanev, *Phys. Lett. B* **219** (1989) 375.
30. T.K. Gaisser, *Vulcano 1992, Proceedings, Frontier objects in astrophysics and particle physics* (1992) 433-445.
31. J. Ranft, *Phys. Rev. D* **51** (1995) 64.
32. The MACRO Collaboration (M. Ambrosio et al.), *Phys. Rev. D* **52** (1995) 3793.

35. A. Fassó et al., "FLUKA: present status and future developments", *Proc. of the IV Int. Conf. on Calorimetry in High Energy Physics,* La Biodola (Is. d'Elba), Italy, 1993, (ed. World Scientific) 493.
36. NUSEX Collaboration (G. Bologna et al.), *Nuovo Cimento* **Vol.8C** No. 1 (1985) 76.
37. D.B. Kieda, PHD thesis, University of Utah (1989).
38. F. James, MINUIT reference manual, CERN, (1994)
39. B. Peters, *Proc. 6th Int. Cosmic Ray Conf., Moscow,* **3** (1959) 157; *Nuovo Cimento,* **22** (1961) 800
40. JACEE Collaboration (T.H. Burnett et al.): Ap.J., **349** (1990) L25; *Proc. of 23rd Int. Cosmic Ray Conf., Calgary,* 2 (1993) 5, 21, 25
41. I.P Ivanenko et al., *Proc. 22nd Int. Cosmic Ray Conf., Dublin,* **2** (1991) 17
42. CRN collaboration, D. Muller et al., *Ap.J.* **374** (1991) 356
43. B. Wiebel-Sooth B. et al., *Proc. of 24th Int. Cosmic Ray Conf., Rome,* 2 (1995) 656
44. N.L. Grigorov et al., *Proc. of 12th Int. Cosmic Ray Conf., Hobart,* 5 (1971) 1746
45. T.V. Danilova, A.D. Erlykin and J. Procureur, *J. Phys. G: Nucl. Part. Phys.* **19** (1993) 429
46. P. Stavrev, N. Gavritova-Stavreva and S. Petrov, *J. Phys. G: Nucl. Part. Phys.* **18** (1992) 1833
47. D.J. Bird et al., *Ap. J.*, **424** (1994) 491; P. Sokolsky, *Proc. of 23rd Int. Cosmic Ray Conf., Calgary,* Invited, Rapporteur & Highlight Papers, World Scientific, ed. D.A. Lealy, R.B. Hicks and D. Venkatesan, p. 447 (1993).
48. S.P. Swordy, *Proc. of 24th Int. Cosmic Ray Conf., Rome,* 2 (1995) 697
49. F. James, "Function Minimization",CERN 72-21 (1972).